COMPUTATIONAL TECHNIQUES USED FOR VELOCITY PREDICTION OF WING-SAILED HYDROFOILING CATAMARANS

MARINE 2017

RICHARD GJ FLAY*, NILS HAGEMEISTER†

* Yacht Research Unit
University of Auckland
Private Bag 92019, Auckland 1142, New Zealand
E-mail: r.flay@auckland.ac.nz, www.yru.auckland.ac.nz

† Formerly Yacht Research Unit Auckland
University of Auckland
Private Bag 92019, Auckland 1142, New Zealand
E-mail: nhag107@aucklanduni.ac.nz

Key words: Multihull, Catamaran, Velocity Prediction, VPP, Foiling, Wing-sails

1 INTRODUCTION

Velocity Prediction Programs (VPP) are among the most commonly used tools in racing yacht design. Whether looking at a parameter-based variant with few degrees of freedom or a full 6 DOF experimental/CFD data postprocessor, their output is often critical to design decisions. In the past, research in this area has mostly concentrated on monohulls, since most major regattas were sailed in these boats.

Following the 34th America's Cup, (foiling) multihulls have moved into the focus of elite sailors and designers. However, publically available information on velocity prediction for these boats remains relatively sparse, especially if resources do not allow for extensive wind tunnel or RANS-CFD studies. Hence the computational techniques used in this study are deliberately restricted to freely available software and self-programmed code that can be run on a standard desktop computer.

2 FORCE DECOMPOSITION

VPPs are essentially optimisation tools for the determination of trim settings for the objective of maximum speed under the constraint of the equilibrium of forces and moments acting on the yacht, as expressed in Eq. (1).

$$\sum F = \sum M = 0 \tag{1}$$

To apply the constraints, these forces have to be modelled, for which they are decomposed according to the fluid they operate in and the part of the boat they apply to.

Figure 1 shows the forces acting on the catamaran as considered in this study. The model assumes linearity of forces and small heel angles, since the righting moment is at its maximum with the windward hull just clearing the water or during level foiling. As a result vertical

aerodynamic forces can be omitted and the vertical position of the centre of gravity becomes irrelevant.

Aerodynamic forces are divided into wing and windage forces. Hydrodynamic forces are split into the contributions from the hull, daggerboard and rudder. For these the inclusion of the vertical forces is particularly important to simulate the foiling states. Dynamic lift on the hull is neglected since it is assumed to be small compared to static buoyancy and the forces exerted by the appendages plus the small error only applies to non-foiling states.

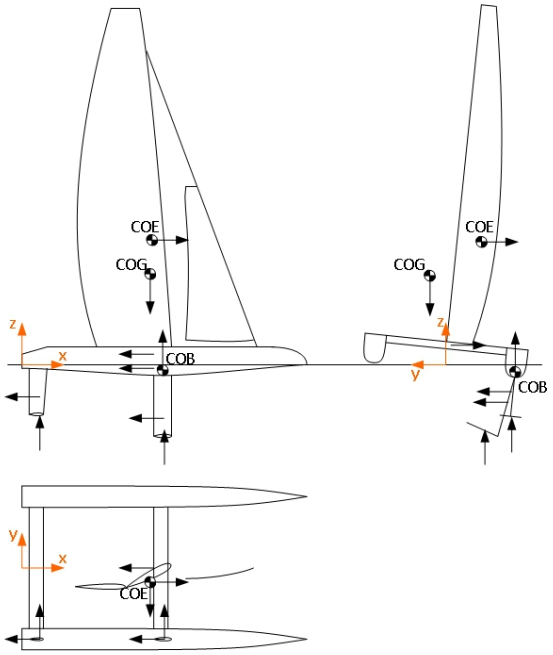

Figure 1: Mechanic model of the catamaran

3 WINDAGE

The windage force is calculated as the product of force coefficient, dynamic pressure and area, as shown in Eq. (2). This universal approach is adapted for each of the three groups into which individual parts are divided depending on their geometrical characteristics.

$$F_i(z_i) = c_{Fi} * \frac{\rho}{2} * AWS(z_i) * A_i \tag{2}$$

Group one contains cables and parts with circular cross-sections and small diameters in relation to their length. For these items two dimensional, laminar flow can be assumed [1], giving a force coefficient of 1.1. Changes in apparent wind speed with height are incorporated through vertical segmentation and calculation of projected areas.

The second group consists of so-called platform components, whose main extents lie in a plane approximately parallel to the water surface. Hence hulls, beams, crew and the bowsprit are believed to be affected by constant apparent wind. The treatment of these parts is inspired by a method commonly used for monohulls [1], which was modified to account for the characteristics of the catamaran. Forces are considered to act on projected frontal and lateral areas independent of the wind angle. For the lateral projected area, which changes with the wind

angle, a conservative estimation of twice the area of a single hull has been used, as it is not clear how much flow reestablishment the separation distance between the hulls allows. A force coefficient of 0.6 was used for group two as suggested by FOSSATI [1]. Furthermore the lateral windage force is taken into account in this study since it influences the side force that has to be produced by the appendages.

Group three contains mostly smaller pieces of equipment and other items with unknown aerodynamic characteristics. Their contribution is estimated at ten percent of platform windage.

4 LIFTING LINE METHODS

4.1 Wing Forces

To capture the effects of flow around wings of finite span and the variation of apparent wind with height as well as the planform and trim of the wing, the forces acting on the wing are calculated by means of a lifting line method as described by GRAF et al. **[2]**, which is summarised in the following.

Lifting Line methods are the expansion of the Kutta-Joukowski-theorem into the third dimension. The lifting vortex is elongated normal to the aerofoil section, resulting in a vortex filament. At the wing tips this vortex filament is aligned with the incident flow and extended to infinity to satisfy Thompson's law. The result is a so-called horseshoe vortex consisting of the bound vortex and two free vortex filaments. Changes in lift are modelled by altering vorticity through shedding of a free vortex filament **[3]**. A vortex sheet is created by decreasing the distance between two neighbouring free vortex filaments to zero. The influence of shed vorticity is expressed as velocity induced normal to incident flow and span, which reduces the effective angle of attack. The approach presented below assumes a bound vortex parallel to the vertical axis which simplifies the mathematics, but restricts the longitudinal alignment of the wing sections and the rake of the wing.

Figure 2 illustrates the discretisation of the wing. A horseshoe vortex consisting of the bound vortex along the quarter-chord line and the root and tip vortices represents the basis. Vortex sheets are distributed at constant intervals along the bound vortex, forming panels limited by

their upper and lower borders. The induced velocity is calculated at collocation points positioned in each panel's vertical centre.

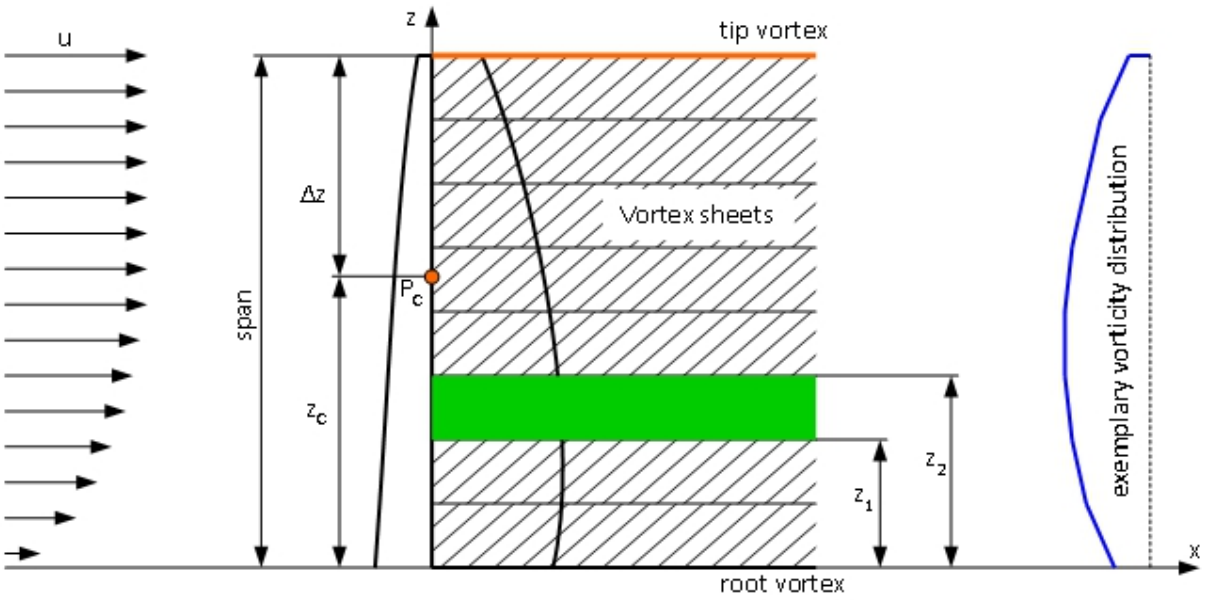

Figure 2: Wing discretisation

Biot-Savart's law is applied to determine the influence of a free vortex (orange highlighting) filament in collocation point P_c [4], Eq. (3).

$$v_{indC} = -\frac{1}{4\pi}\frac{\Gamma}{\Delta z} \tag{3}$$

The effect of a vortex sheet created by the linear change in vorticity (Γ_2-Γ_1) between z_1 and z_2 is computed by Eq. (4) [2].

$$v_{indC} = -\frac{1}{4\pi} * \frac{\Gamma_2 - \Gamma_1}{r_2 - r_1} \ln\left(\frac{z_2 - z_C}{z_1 - z_C}\right) \tag{4}$$

The total velocity induced at P_c is calculated as the sum of the induced velocities of all panels plus the contributions of the root and tip vortices. Self-induction is excluded since the natural logarithm is not defined for a negative argument. To model the weakening of the root vortex through the endplate effects of the platform, the factor EP is adopted [2], Eq. (5).

$$v_{indCj} = \left[\sum_{i=1}^{N,i\neq j} -\frac{1}{4\pi} * \frac{\Gamma_i - \Gamma_{i-1}}{z_i - z_{i-1}} \ln\left(\frac{z_i - z_{Cj}}{z_{i-1} - z_{Cj}}\right)\right] - EP\frac{1}{4\pi}\frac{\Gamma_0}{(z_0 - z_{Cj})} + \frac{1}{4\pi}\frac{\Gamma_N}{(z_N - z_{Cj})} \tag{5}$$

Eq. (5) can be rewritten by summarising the geometric relations into factors, Eq. (6).

$$\left[\sum_{i=1}^{N,i\neq j} -\frac{1}{4\pi} * \Gamma_i - \Gamma_{i-1} * \mathrm{f_{sheetij}}\right] - EP\frac{\Gamma_0}{4\pi} f_{rootj} + \frac{\Gamma_N}{4\pi} f_{tipj} \tag{6}$$

Since the induced velocities have to be known at the boundaries of each centre to determine the vorticities for the next iteration, induced velocities are interpolated from two neighbouring panels. At the root and tip of the wing they are extrapolated [2], as shown in Eqs. (7-9).

$$v_{indi} = \frac{(v_{indCi+1} + v_{indCi})}{2} \tag{7}$$

$$v_{ind0} = 2v_{indC1} - v_{ind1} \tag{8}$$

$$v_{indN} = 2v_{indCN-1} - v_{indN-1} \tag{9}$$

Vorticity is derived from Kutta's law which specifies lift as the product of density, velocity and vorticity and the equivalent definition of lift as function of lift coefficient, dynamic pressure and reference area [2], Eq. (10).

$$L = \rho_{air} * u * \Gamma = \frac{\rho}{2} * u^2 * A * c_L \tag{10}$$

The lift coefficient depends on the Reynolds number and the angle of attack, which is affected by the induced velocities [2], as shown in Eq. (11).

$$AoA_{eff} = \mathrm{AoA} - \frac{v_{ind}}{u} \tag{11}$$

Combining Eqs. (10) and (11) results in Eq. (12) [2].

$$\Gamma = \frac{u}{2} * A * c_L\left(AoA - \frac{v_{ind}}{u}, Re\right) \tag{12}$$

Induced drag is proportional to the ratio of induced to incident velocity and lift. Parasitic profile drag is added to obtain total drag [2]. The required drag coefficient is obtained by interpolating in a table listing it as function of angle of attack and the Reynolds number, Eq. (13).

$$D_{total} = \frac{v_{ind}}{u} * L + \frac{\rho_{air}}{2} * u^2 * A * c_{Dpp}(AoA_{eff}, Re) \tag{13}$$

To enable trimming of the wing two parameters have been introduced. The angle between the root section and centreline of the yacht is denoted as α_{CL} whereas twist is defined as the angle differential between root and tip section. Twist is varied linearly along the span, Eq. (14).

$$AoA(z) = AWA(z) - a_{CL} - \frac{twist}{span} * (z - z_0) \tag{14}$$

Since the wing operates within the part of the planetary boundary layer with the highest velocity gradients, its vertical position can be altered according to the elevation of the platform.

4.2 Appendage forces

The forces produced by the appendages are calculated with a lifting line approach similar to that presented in Section 4.1. However, since the appendages are non-planar wings, a three-dimensional approach has been selected. Additionally, the boundary conditions have been revisited to incorporate effects of surface proximity and surface piercing when foiling.

In contrast to the vortex sheets of wing, the appendages are modelled by horseshoe vortices distributed along the span. This choice has been made to simplify the mathematical

relationships in the third dimension. The reduction in accuracy is compensated for by an increase in the number of panels. Figure 3 shows the discretisation of a three-dimensional wing.

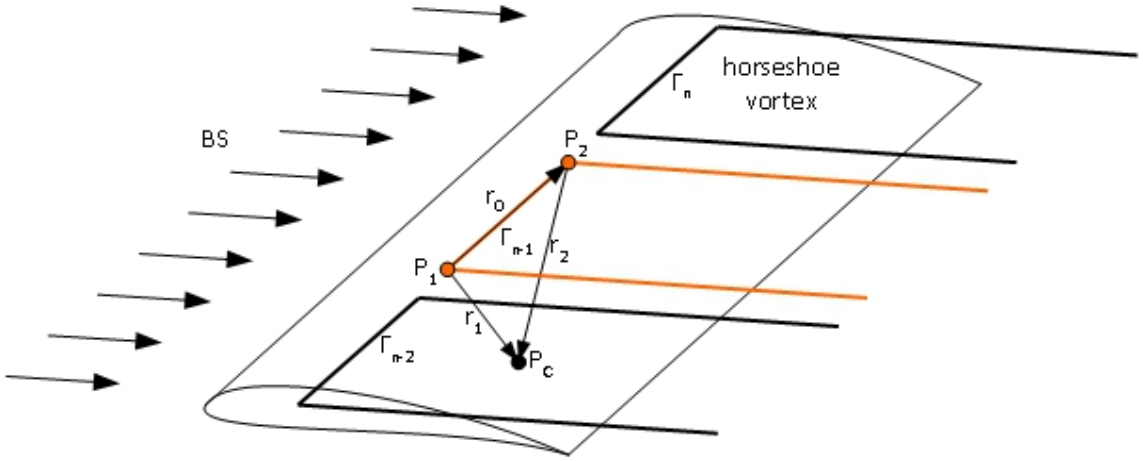

Figure 3: Discretization of appendages wing

Induced velocities are calculated from the three dimensional form of the Biot-Savart-law [4], Eq. (15).

$$\overrightarrow{v_{ind}} = \frac{\Gamma}{4\pi}\int_f \frac{\vec{r} \times \overrightarrow{ds}}{|r|^3} \tag{15}$$

Using the definitions from figure 3 Eq. (15) can be rewritten [4] as Eq. (16).

$$\overrightarrow{v_{ind}} = \frac{\Gamma_{n-1}}{4\pi}\frac{(\overrightarrow{r_1} \times \overrightarrow{r_2})}{|\overrightarrow{r_1} \times \overrightarrow{r_2}|^2} * \overrightarrow{r_0} * \left(\frac{\overrightarrow{r_1}}{|\overrightarrow{r_1}|} - \frac{\overrightarrow{r_2}}{|\overrightarrow{r_2}|}\right) \tag{16}$$

The expression is transformed into Eq. (17) to avoid the singularity that occurs when vectors $\overrightarrow{r_1}$ and $\overrightarrow{r_2}$ are parallel [5].

$$\overrightarrow{v_{ind}} = \frac{\Gamma_{n-1}}{4\pi}\frac{(|\overrightarrow{r_1}| + |\overrightarrow{r_2}|)(\overrightarrow{r_1} \times \overrightarrow{r_2})}{|\overrightarrow{r_1}||\overrightarrow{r_2}| * (|\overrightarrow{r_1}| * |\overrightarrow{r_2}| + \overrightarrow{r_1} * \overrightarrow{r_2})} \tag{17}$$

To avoid the singularity in the Biot-Savart-law for distances approaching zero and improve numerical stability, two factors k_i and k_{bi} are introduced that gradually reduce the influence of the vortices when in close proximity to each other [6]. e_{core} denotes the diameter of the viscous vortex core and was set to 0.01 m for this study. A value of 2 was selected for m in Eq. (18) based on the recommendations of ABEDI [6].

$$k_i = \frac{\left(\frac{|\overrightarrow{r_i} \times \overrightarrow{BS}|}{|\overrightarrow{BS}|}\right)^m}{\left(e_{core}^{2m} + \left(\frac{|\overrightarrow{r_i} \times \overrightarrow{BS}|}{|\overrightarrow{BS}|}\right)^{2m}\right)^{\frac{1}{m}}} \tag{18}$$

$$k_b = \frac{\left(\frac{|\vec{r_1} \times \vec{r_0}|}{|\vec{r_0}|}\right)^m}{\left(e_{core}^{2m} + \left(\frac{|\vec{r_1} \times \vec{r_0}|}{|\vec{r_0}|}\right)^{2m}\right)^{\frac{1}{m}}} \tag{19}$$

Using the notation from figure 3 and applying Eqs. (18) and (19) to the bound and free vortex filaments, an expression for the total influence of a horseshoe vortex can be derived [5], Eq. (20).

$$\overrightarrow{v_{\iota,n-1}} = \frac{\Gamma_{n-1}}{4\pi}\left[k_2 \frac{\left(\frac{\overrightarrow{BS}}{|\overrightarrow{BS}|} \times \vec{r_2}\right)}{|\vec{r_2}| * \left(|\vec{r_2}| - \frac{\overrightarrow{BS}}{|\overrightarrow{BS}|} * \vec{r_2}\right)} + k_b \frac{(|\vec{r_1}| + |\vec{r_2}|)(\vec{r_1} \times \vec{r_2})}{|\vec{r_1}||\vec{r_2}| * (|\vec{r_1}||\vec{r_2}| + \vec{r_1} * \vec{r_2})} - k_1 \frac{\left(\frac{\overrightarrow{BS}}{|\overrightarrow{BS}|} \times \vec{r_1}\right)}{|\vec{r_1}| * \left(|\vec{r_1}| - \frac{\overrightarrow{BS}}{|\overrightarrow{BS}|} * \vec{r_1}\right)}\right] \tag{20}$$

Again the geometrical relationships can be factored out, transforming Eq. (20) to Eq. (21).

$$\overrightarrow{v_{\iota,n-1}} = \frac{\Gamma_{n-1}}{4\pi} * f_{n-1} \tag{21}$$

The total induced velocity at point P_C is the sum of the velocities induced by each individual horseshoe vortex, as expressed in Eq. (22).

$$\vec{v_\iota} = \sum_{j=1}^{n} \overrightarrow{v_{\iota,j}} \tag{22}$$

Local flow conditions are determined by the total induced velocity to the incident flow.

$$\vec{w_\iota} = \overrightarrow{BS} + \overrightarrow{v_{\iota ndC}} \tag{23}$$

The angle of attack is derived using vector calculus, as in Eq. (24). $\vec{q_\iota}$ and $\vec{c_\iota}$denote the vectors normal to the wing surface and along the chord, respectively [5].

$$AoA_i = \tan^{-1}\left(\frac{\vec{w_\iota} * \vec{q_\iota}}{\vec{w_\iota} * \vec{c_\iota}}\right) \tag{24}$$

Equating the three dimensional form of the Kutta-Joukowski-theorem [4] with the well-known formula defining lift as the product of lift coefficient, dynamic pressure and area yields an expression to calculate vorticity, as shown in Eq. (25). $\vec{s_\iota}$ represents the vector along the span of the wing section.

$$\frac{\rho_{water}}{2} * BS^2 * A_i * c_{L_i} = |\Gamma_i * \rho_{water} * \vec{w_\iota} \times \vec{s_\iota}| \tag{25}$$

Introducing local chord c_i and span s_i Eq. (25) can be transformed to Eq. (26).

$$\frac{1}{2} * BS^2 * s_i * c_i * c_{L_i} = |\Gamma_i * \vec{w_\iota} \times \vec{s_\iota}| \tag{26}$$

Since vorticity has to be proportional to the lift coefficient, Eq. (26) can be transposed to result in the formula used to calculate vorticity, Eq. (27).

$$\Gamma_i = \frac{0.5 * BS^2 * s_i * c_i * c_{L_i}}{|\overrightarrow{w_i} \times \overrightarrow{s_i}|} \tag{27}$$

The total force exerted by a profile section is the sum of the parasitic profile drag and the force derived from the Kutta-Joukowski-theorem, Eq. (28).

$$\overrightarrow{F_i} = \overrightarrow{D_{ppi}} + \rho_{water} * \Gamma_i \times \left(\overrightarrow{BS} + \overrightarrow{v_i}\right) \tag{28}$$

Parasitic profile drag is calculated as the product of dynamic pressure, area and drag coefficient acting along the direction of the incident flow, as given in Eq. (29).

$$\overrightarrow{D_{pp}} = c_{Dpp}\left(AoA_{eff}, Re\right) * \frac{\rho_{water}}{2} * \left|\overrightarrow{BS}\right|^2 * A_i * \frac{\overrightarrow{BS}}{\left|\overrightarrow{BS}\right|} \tag{29}$$

The effects of surface proximity have to be considered for the appendages. Since the surface represents a constant pressure boundary, the pressure fields of the appendages deform the water surface [7]. As a result transverse waves are formed and the extents of the pressure fields are reduced. The latter is often modelled by virtual mirroring of the foil at the water surface to cancel out the foil's influence. This approach neglects the deformation of the water surface, which can be justified by the long wavelength associated with high Froude numbers [8]. Hence the total induced velocity calculated in Eq. (22) has to be amended by the contribution of the mirror image, as shown in Eq. (30).

$$\overrightarrow{v_i} = \sum_{j=1}^{n} \overrightarrow{v_{i,J}} + \sum_{j=1}^{n} \overrightarrow{v_{mi,J}} \tag{30}$$

Since the densities of water and air differ by a factor of approximately 10^3, surface piercing states are modelled by setting the density of airborne sections to zero.

4.3 Implementation

Since the given equations are not independent of each other, the solution has to be found iteratively. The computation sequence given in [2] has been slightly modified from the original to reduce runtime in the present work. The sequence of computation steps is given below.

1. Assign geometric properties and apparent incident velocity to each profile section.
2. Calculate matrix of influence factors from geometric relations.
3. Determine angle of attack and derive lift coefficient for each section.
4. Obtain section vorticity from lift coefficient
5. Compute total velocity induced in each panel using geometric influence factors.
6. Check convergence criteria and repeat steps 3.-5. if necessary.
7. Calculate section lift
8. Calculate induced and parasitic drag.
9. Determine driving and side forces from sectional lift, drag and AWA and integrate forces over span.

Since the method is only valid for primarily two-dimensional flow [2], stall has to be avoided, because of separated flow having a pronounced three dimensional flow pattern. To reduce the chance of trim optimisation leading to stalled wing sections, the progression of

the lift curve was altered. Figure 4 shows an exemplary comparison between the real trend of the lift coefficient as a function of angle of attack and the altered curve used for this study. It can be seen that in reality the lift drops somewhat after the stall angle is reached. The lift then starts to increase again after a local minimum is passed. The modified curve passes the local minimum and continues its descent until zero.

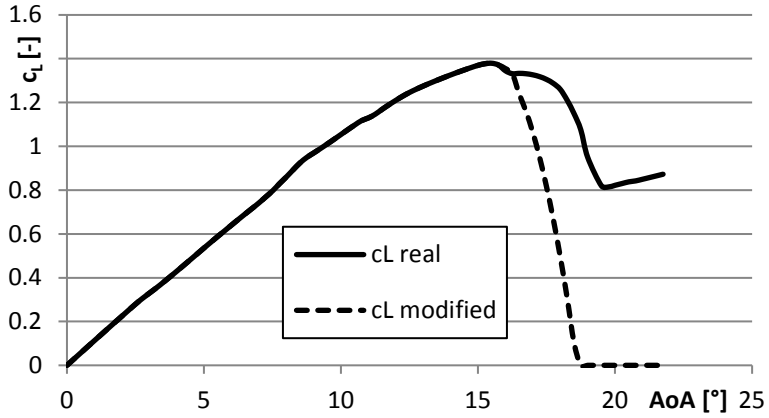

Figure 4: Comparison of real and modified lift curves

According to GRAF et al [2] the iterative process needs under-relaxation in order to achieve convergence. Under-relaxation factors of ω = 0.1 for the wing and ω = 0.05 for the appendages have been selected and used in Eq. (31).

$$v_{ind} = \overbrace{v_{ind}\omega}^{current\ step} + \overbrace{v_{ind}(1-\omega)}^{last\ step} \tag{31}$$

5 HULL RESISTANCE

Hull resistance can be is split into frictional, wavemaking and viscous pressure components. In this study friction is assessed by applying the ITTC'57 friction line using the static wetted surface area.

For the computation of wavemaking drag OLIVER [9] suggested using the theory developed by MICHELL. His approach belongs to the group of slender ship theories to which the hulls concerned in this study seem ideally suited, with slenderness and length to beam ratios of 11.7 and 17.6, respectively. One disadvantage arising from this choice is the neglect of viscous pressure resistance, since this is not captured in the theory. For more details the reader is referred to [10]

MICHELL's theory is implemented into the potential flow research code *Michlet*, which was developed by CYBERIAD [10].

Figure 5 shows a comparison of predicted resistance using friction line and panel code to experimental towing tank data of a Tornado class catamaran hull. The resistance hump around hull speed is well captured. Although there is generally good agreement between the datasets up to a Froude number of around 0.8, the disparity between calculated wave-making resistance and measured residuary resistance increases with speed. This is in accordance with expectations since viscous pressure resistance is caused by the loss in momentum through friction, whose

share of the overall increases with speed. Hence, viscous pressure resistance will increase with speed as well. This relationship is also indicated by the shape of the curves with the predicted wave-making drag exhibiting asymptotic behaviour at high Froude numbers, while the residuary resistance values seem to follow the frictional resistance graph.

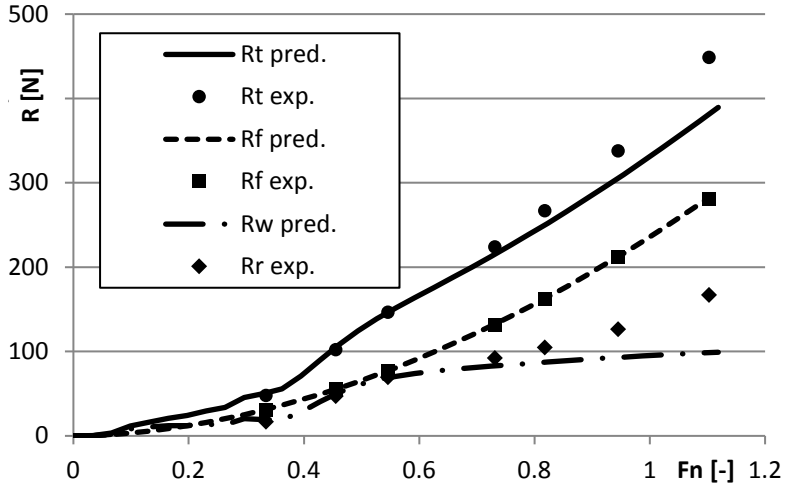

Figure 5: Comparison of predicted and experimental resistance data

Similar to the hydrostatic forces, the resistance of the hull has to be known as a function of the draft in order to be able to model the yacht's transition to foiling. Hence resistance curves have been calculated for different drafts. The results are shown in figure 6 for a range of drafts between 0.05 m and 0.45 m.

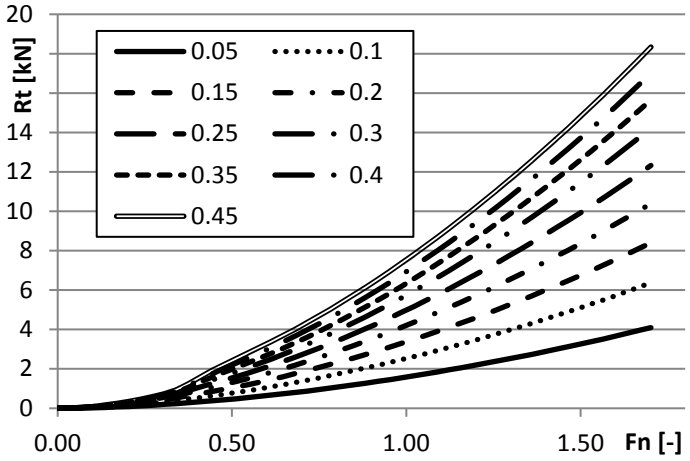

Figure 6: Hull resistance curves for range of drafts

6 RESULTS

The models have been integrated into a VPP which has been implemented as a constraint optimisation routine in Matlab. Figure 7 shows a polar plot of the VPP outputs for 4 different wind speeds. It can be seen that speeds of the order of up to 2.5 times wind speed are reached.

It can be seen that an increase in wind speed and true wind angle creates the desired effect of an increase in boat speed. This trend continues until the wing lift cannot be increased by an increase in angle of attack anymore, or the minimum heeling moment constraint cannot be satisfied anymore. Furthermore, the transition to foiling can be clearly identified as distinct jumps in speed in two of the curves.

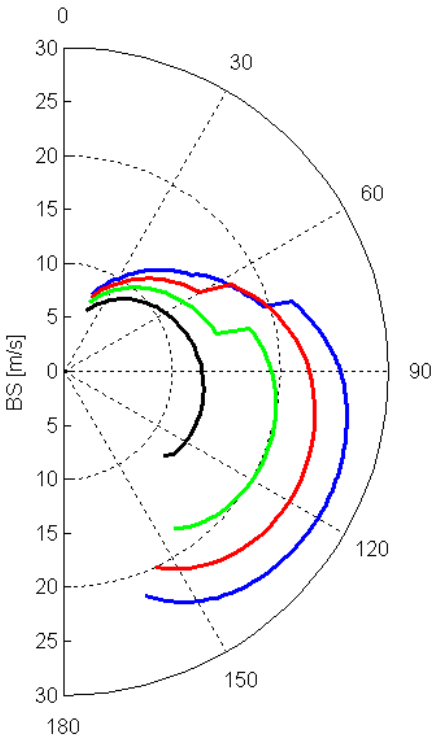

Figure 7: Speed polar plot for windspeeds of 5.0m/s (black), 7.5m/s (green), 10.0m/s (red) and 12.5m/s (blue)

7 CONCLUSIONS

- Different models aimed at the calculation of forces for the velocity prediction of catamarans have been presented.
- The results of the velocity prediction are encouraging for further research.
- The hardware demands of all models are such that they can be run on standard desktop computers and still deliver results within a fraction of a second.
- Apart from Matlab, only free software is used, limiting the required resources required to achieve useful VPP predictions.

REFERENCES

[1] F. Fossati, Aero-Hydrodynamics And The Performance of Sailing Yachts, London, Great Britain: Adlard Coles Nautical, 2009.

[2] K. Graf, A. van Hoeve and S. Watin, "Comparison Of Full 3D-RANS Simulations with 2D-RANS/Lifting Line Method Calculations For The Flow Analysis Of Rigid Wings For High Performance Multihulls," in *3rd International Conference on Innovation in High Performance Sailing Yachts (INNOV'SAIL)*, Lorient, France, 2013.

[3] I. H. Abbott and A. E. von Doenhoff, Theory Of Wing Sections, New York, USA: Dover Publications, Inc., 1959.

[4] J. Katz and A. Plotkin, Low-Speed Aerodynamics, Singapore: McGraw-Hill, Inc., 1991.

[5] W. Phillips and D. Snyder, "Modern adaption of Prandtl's classic lifting line theory," *Journal of Aircraft, Vol. 37, No. 4,* pp. pp. 662-670, 2000.

[6] H. Abedi, "Development of Vortex Filament Method for Aerodynamic Loads on Rotor Blades," Chalmers University of Technology, Department of Applied Mechanics, Gothenburg, Sweden, 2013.

[7] M. Daskovsky, "The hydrofoil in surface proximity," *Ocean Engineering 27,* pp. pp. 1129-1159, 2000.

[8] L. G. Straub, "Experimental And Analytical Studies Of Dihedral Hydrofoils," St. Anthony Falls Hydraulic Laboratory, Minneapolis, USA, 1954.

[9] C. Oliver, "Performance Prediction Method for Multihull Yachts," in *Proceedings of the 9th Chesapeake Sailing Yacht Symposium*, Annapolis, USA, 1989.

[10] Cyberiad, "MICHLET 9.32 User's Manual," Cyberiad, provided with the Michlet 9.32 Research Code which can be downloaded from http://www.cyberiad.net/michlet.htm, 2014.